A robust reconstruction for unstructured WENO schemes[1]

Yuan Liu[2] and Yong-Tao Zhang[3*]

*Corresponding author. Tel.: +1 574 631 6079. E-mail: yzhang10@nd.edu

Abstract

The weighted essentially non-oscillatory (WENO) schemes are a popular class of high order numerical methods for hyperbolic partial differential equations (PDEs). While WENO schemes on structured meshes are quite mature, the development of finite volume WENO schemes on unstructured meshes is more difficult. A major difficulty is how to design a robust WENO reconstruction procedure to deal with distorted local mesh geometries or degenerate cases when the mesh quality varies for complex domain geometry. In this paper, we combine two different WENO reconstruction approaches to achieve a robust unstructured finite volume WENO reconstruction on complex mesh geometries. Numerical examples including both scalar and system cases are given to demonstrate stability and accuracy of the scheme.

Key Words: Weighted essentially non-oscillatory (WENO) schemes, finite volume schemes, high-order accuracy, unstructured meshes.

AMS(MOS) subject classification: 65M99

[1]This research was supported by NSF grant DMS-0810413.

[2]Department of Applied and Computational Mathematics and Statistics, University of Notre Dame, Notre Dame, IN 46556, USA. E-mail: yliu7@nd.edu

[3]Department of Applied and Computational Mathematics and Statistics, University of Notre Dame, Notre Dame, IN 46556, USA. E-mail: yzhang10@nd.edu

1 Introduction

Weighted essentially non-oscillatory (WENO) schemes are a class of high order numerical methods for solving partial differential equations (PDEs) whose solutions may contain discontinuities, sharp gradient regions, and other complex solution structures. They are designed based on the successful ENO schemes in [9, 19]. The first WENO scheme was constructed in [13] for a third order finite volume version. In [12], third and fifth order finite difference WENO schemes in multi-space dimensions were constructed, with a general framework for the design of the smoothness indicators and non-linear weights. The main idea of the WENO scheme is to form a weighted combination of several local reconstructions based on different stencils (usually referred to as small stencils) and use it as the final WENO reconstruction. The combination coefficients (also called non-linear weights) depend on the linear weights, often chosen to increase the order of accuracy over that on each small stencil, and on the smoothness indicators which measure the smoothness of the reconstructed function in the relevant small stencils. Hence an adaptive interpolation or reconstruction procedure is actually the essential part of the WENO schemes.

WENO schemes have the advantage of attaining uniform high order accuracy in smooth regions of the solution while maintaining sharp and essentially monotone shock transitions. While finite differece WENO schemes on structured meshes have been developed and studied extensively [12, 17, 10, 22, 6, 2, 14], the development of WENO schemes on unstructured meshes (e.g. triangular or tetrahedral meshes) for dealing with complex domain geometries is less advanced. Since the finite difference approach [12] requires mesh smoothness and cannot be used on unstructured meshes while maintaining local conservation, we must use the more complicated and more costly finite volume approach [13, 11, 18].

There are two types of finite volume WENO schemes on unstructured meshes in the literature. The first type (type I) consists of WENO schemes whose order of accuracy is not higher than that of the reconstruction on each small stencil. This is similar as ENO schemes. For this type of WENO schemes, the non-linear weights do not contribute towards

the increase of the order of accuracy, and they are designed purely for the purpose of nonlinear stability, or to avoid spurious oscillations. Because type I WENO schemes just need to choose the linear weights as arbitrary positive numbers for better linear stability (e.g. the centered small stencil is assigned a larger linear weight than the others), they are easier to construct than the type II WENO schemes discussed in the following paragraph. Type I WENO schemes include the WENO schemes in [7, 20] for two dimensional (2D) triangulations and in [3, 4] for three dimensional (3D) triangulations.

The second type (type II) consists of WENO schemes whose order of accuracy is higher than that of the reconstruction on each small stencil. For example, the third order WENO scheme on 2D triangular meshes in [11] is based on second order linear polynomial reconstructions on small stencils, and the fourth order WENO scheme in [11] is based on third order quadratic polynomial reconstructions on small stencils. See also [23] for similar WENO schemes on 2D triangular meshes for solving Hamilton-Jacobi equations, which belong to type II as well. On 3D tetrahedral meshes, type II WENO schemes were constructed in [24], and Hermite WENO schemes were developed in [27]. Type II WENO schemes are more difficult to construct, however they have a more compact stencil than type I WENO schemes of the same accuracy, which is an advantage in some applications, such as when the WENO methodology is used as limiters for the discontinuous Galerkin methods [15, 16, 25, 26].

A crucial step in building a type II WENO scheme on unstructured meshes is to construct lower order polynomials whose weighted average will give the same result as the high order reconstruction at each Gaussian quadrature point for the flux integral on the element boundary. This step is actually the most difficult step in designing a robust second type high order WENO schemes on unstructured meshes, since we can not guarantee the quality of the unstructured meshes when the domain geometry is very complicated. The local linear system for finding linear weights could have very large condition number or is even singular at the places where mesh quality is bad (e.g. there are very obtuse triangles). Directly solving the ill-posed local linear system leads to very negative large linear weights and instability

can appear even if we use the procedure to deal with the negative linear weights as in [18]. Specifically, the problems needed to be solved are: how to find linear weights for distorted local mesh geometries? how to deal with the degenerate cases which could happen when the mesh quality is not good? A robust strategy needs to be developed for finding the linear weights with respect to various mesh geometries. This is even more important for higher order schemes and three dimensional problems.

In this paper, we hybrid the approaches of type II and type I WENO schemes, and avoid the appearance of very negative large linear weights no matter the quality of the unstructured meshes. The idea is to switch to the approach of assigning linear weights of type I WENO schemes at the places where the linear weight system of type II WENO scheme is ill-posed or singular, i.e., the linear weights do *not* exist or are very negative large, i.e., larger than a preset threshold value. The tradeoff is that the compactness of the type II WENO scheme will be lost at these places. But we will obtain a robust reconstruction with respect to the quality of unstructured meshes and the complexity of the domain. Furthermore, the overall percentage of the places where the type I WENO approach is applied is quite small, according to our numerical experiments in this paper.

The organization of this paper is as follows. The algorithm is developed in section 2. Section 3 contains extensive numerical examples verifying stability, convergence and accuracy of the algorithm, on unstructured meshes including meshes with distorted local mesh geometries. Concluding remarks are given in section 4.

2 A robust unstructured WENO reconstruction

In this paper we use two-dimensional problems to test the proposed hybrid method. But this method can also be applied to higher dimensional problems straightforwardly.

2.1 The finite volume formulation on 2D triangular meshes

We solve the two-dimensional conservation law

$$\frac{\partial u}{\partial t} + \frac{\partial f(u)}{\partial x} + \frac{\partial g(u)}{\partial y} = 0 \tag{2.1}$$

using the finite volume formulation as in [11]. Computational control volumes are triangles.

Taking the triangle $\triangle_i$ as our control volume, we formulate the semi-discrete finite volume scheme of (2.1) as

$$\frac{d\bar{u}_i(t)}{dt} + \frac{1}{|\triangle_i|}\int_{\partial\triangle_i} F \cdot n dS = 0 \tag{2.2}$$

where the cell average $\bar{u}_i(t) = \frac{1}{|\triangle_i|}\int_{\triangle_i} u dxdy$, $F = (f, g)^T$, and n is the outward unit normal of the triangle boundary $\partial\triangle_i$.

In (2.2), the line integral is discretized by a q-point Gaussian quadrature formula,

$$\int_{\partial\triangle_i} F \cdot n ds \approx \sum_{k=1}^{3} S_k \sum_{j=1}^{q} w_j F(u(G_j^{(k)}, t)) \cdot n_k \tag{2.3}$$

where S_k is the length of the k-th side of $\partial\triangle_i$, $G_j^{(k)}$ and w_j are the Gaussian quadrature points and weights respectively, and $F(u(G_j^{(k)}, t)) \cdot n_k$ is approximated by a numerical flux. We use the Lax-Friedrichs flux in this paper, which is given by

$$F(u(G_j^{(k)}, t))\cdot n_k \approx \frac{1}{2}\left[\left(F(u^-(G_j^{(k)}, t)) + F(u^+(G_j^{(k)}, t))\right) \cdot n_k - \alpha\left(u^+(G_j^{(k)}, t) - u^-(G_j^{(k)}, t)\right)\right], \tag{2.4}$$

where α is taken as an upper bound for the magnitude of the eigenvalues of the Jacobian in the n_k direction, and u^- and u^+ are the values of u inside the triangle and outside the triangle (inside the neighboring triangle) at the Gaussian point.

In this paper we use a third order finite volume scheme to test our hybrid WENO reconstruction procedure, so the two-point Gaussian quadrature $q = 2$ is used. For the line with endpoints P_1 and P_2, the Gaussian quadrature points are $G_1 = cP_1 + (1-c)P_2$, $G_2 = cP_2 + (1-c)P_1$, where $c = \frac{1}{2} + \frac{\sqrt{3}}{6}$; and the Gaussian quadrature weights are $w_1 = w_2 = \frac{1}{2}$.

2.2 WENO reconstruction

The key step in finite volume WENO schemes is to build a high order WENO reconstruction for the point values at the Gaussian quadrature points. The big stencil S in a WENO reconstruction is a union of small stencils $\{S_m : m = 1, 2, ..., N\}$. Cell average values of u in S are used to construct a polynomial $p(x, y)$, which will have the same cell average as u on the target cell $\triangle_0$ (i.e., the control volume cell). Both type I and type II WENO schemes need to obtain a linear combination of reconstructions on small stencils. The reconstruction values at the Gaussian points should satisfy

$$p(x^G, y^G) = \sum_{m=1}^{N} \gamma_m p_m(x^G, y^G), \tag{2.5}$$

where (x^G, y^G) is a Gaussian point, p_m is a reconstruction polynomial on a small stencil S_m, and γ_m is called a linear weight. The major difference between type I and type II WENO reconstructions is the different method to construct small stencils and find linear weights. We will discuss the details in the following sub-sections. Based on (2.5), nonlinear WENO reconstruction values at the Gaussian points are

$$p_{\text{weno}}(x^G, y^G) = \sum_{m=1}^{N} \omega_m p_m(x^G, y^G), \tag{2.6}$$

where ω_m is a nonlinear WENO weight defined as

$$\omega_m = \frac{\tilde{\omega}_m}{\sum_{m=1}^{N} \tilde{\omega}_m}, \qquad \tilde{\omega}_m = \frac{\gamma_m}{(\epsilon + IS_m)^2.} \tag{2.7}$$

IS_m is the smoothness indicator for the m-th reconstruction polynomial $p_m(x, y)$ associated with the m-th small stencil S_m, and ϵ is a small positive number to aoid the denominator to become 0. We take $\epsilon = 10^{-3}$ for all the computations in this paper. Usually larger ϵ is more friendly for smooth solutions but may generate small oscillations for shock waves, while smaller ϵ is more friendly to shocks. In a range of ϵ from 10^{-2} to 10^{-6}, the numerical results are not very sensitive to ϵ. The smoothness indicator measures how smooth the function p_m is on the target cell $\triangle_0$: the smaller the smoothness indicator, the smoother the function p_m

is on $\triangle_0$. We follow [12, 11] and define it as

$$IS_m = \sum_{1\le|\alpha|\le k} \int_{\triangle_0} |\triangle_0|^{|\alpha|-1} (D^\alpha p_m(x,y))^2 dxdy, \tag{2.8}$$

where k is the degree of polynomial p_m, α is a multi-index and D is the derivative operator.

2.2.1 Type I linear reconstruction

Type I reconstructions for WENO schemes on unstructured meshes were developed in [7, 3, 4, 20]. For example, we can use the big stencil S shown in Figure 2.1 for a third order type I WENO reconstruction. Four small stencils consists of one central stencil S_0 and three sectorial stencils S_i, S_j, S_k. All small stencils include the target cell $\triangle_0$ (the cell "0" as shown in Figure 2.1) which should be at the central position of the big stencil S. The central stencil S_0 includes the target cell $\triangle_0$ and its two layers of neighbors. In Figure 2.1, $S_0 = \{\triangle_0, \triangle_{i_1}, \triangle_{j_1}, \triangle_{k_1}, \triangle_{i_2}, \triangle_{i_3}, \triangle_{j_2}, \triangle_{j_3}, \triangle_{k_2}, \triangle_{k_3}\}$. By connecting the barycenter of $\triangle_0$ with its three vertices, we obtain three lines L_i, L_j and L_k. These three lines partition the domain into three sectors. Every sectorial stencil consists of a few layers of neighboring cells of $\triangle_0$, and the barycenters of these cells fall inside the sector. For a third order reconstruction, we need to reconstruct a quadratic polynomial on each sectorial stencil. As shown in Figure 2.1, the sectorial stencils $S_i = \{\triangle_0, \triangle_{i_1}, \triangle_{i_2}, \triangle_{i_3}, \cdots, \triangle_{i_7}\}$, $S_j = \{\triangle_0, \triangle_{j_1}, \triangle_{j_2}, \triangle_{j_3}, \cdots, \triangle_{j_7}\}$, $S_k = \{\triangle_0, \triangle_{k_1}, \triangle_{k_2}, \triangle_{k_3}, \cdots, \triangle_{k_7}\}$. On each sectorial stencil, we determine a quadratic polynomial by requiring that it has the same cell average as u on $\triangle_0$, and also it matches the cell averages of u on the triangles of the sectorial stencil except $\triangle_0$ in a least-square sense [1]. Notice that we use more than 6 triangles for each sectorial stencil to obtain a quadratic polynomial. The strategy (i.e., to use more elements in the stencil than the minimal required elements) is recommended in the literature (e.g. [7, 3, 4, 20]) for better stability on general meshes. We obtain four quadratic polynomials $p_0(x,y), p_i(x,y), p_j(x,y), p_k(x,y)$ on S_0, S_i, S_j and S_k respectively. A linear reconstruction at the Gaussian points is formed as

$$p(x^G, y^G) = \gamma_0 p_0(x^G, y^G) + \gamma_i p_i(x^G, y^G) + \gamma_j p_j(x^G, y^G) + \gamma_k p_k(x^G, y^G) \tag{2.9}$$

where $\gamma_0, \gamma_i, \gamma_j, \gamma_k$ are the linear weights. As in type I WENO reconstructions, we assign the central stencil a large linear weight $\gamma_0 = 10^3$. Smaller linear weights $\gamma_i = \gamma_j = \gamma_k = 1$ are assigned to the sectorial stencils. Note that the sum of linear weights is not 1 at this time. This problem is automatically solved when the nonlinear WENO weights (2.7) are calculated.

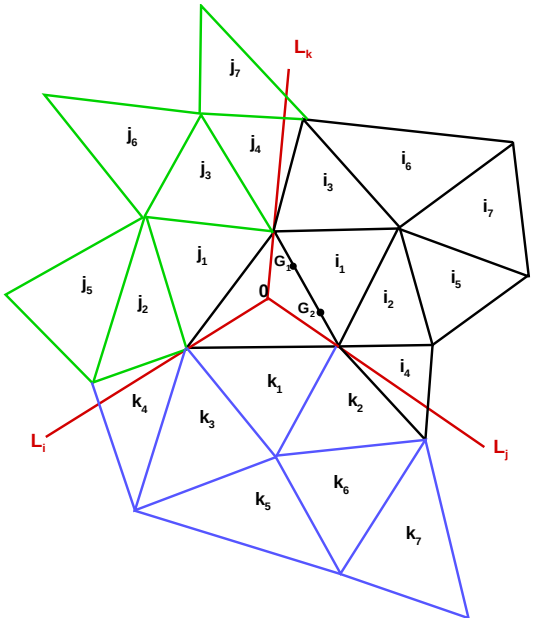

Figure 2.1: A big stencil S for a third order type I WENO reconstruction. Four small stencils consists of one central stencil S_0 and three sectorial stencils S_i, S_j, S_k. All small stencils include the target cell $\triangle_0$ (i.e., the cell "0"). $S_0 = \{\triangle_0, \triangle_{i_1}, \triangle_{j_1}, \triangle_{k_1}, \triangle_{i_2}, \triangle_{i_3}, \triangle_{j_2}, \triangle_{j_3}, \triangle_{k_2}, \triangle_{k_3}\}$; S_i includes the cell $\triangle_0$ and the cells in black color, i.e. $S_i = \{\triangle_0, \triangle_{i_1}, \triangle_{i_2}, \triangle_{i_3}, \cdots, \triangle_{i_7}\}$; S_j includes the cell $\triangle_0$ and the cells in green color, i.e. $S_j = \{\triangle_0, \triangle_{j_1}, \triangle_{j_2}, \triangle_{j_3}, \cdots, \triangle_{j_7}\}$; S_k includes the cell $\triangle_0$ and the cells in blue color, i.e. $S_k = \{\triangle_0, \triangle_{k_1}, \triangle_{k_2}, \triangle_{k_3}, \cdots, \triangle_{k_7}\}$.

2.2.2 Type II linear reconstruction

Type II reconstructions (e.g. [11, 24, 27]) for WENO schemes use a much more compact big stencil. A third order type II WENO scheme on 2D triangular meshes [11] uses a big stencil S as shown in Figure 2.2. It includes the target cell $\triangle_0$ and its two layers of neighbors: $S = \{\triangle_0, \triangle_i, \triangle_j, \triangle_k, \triangle_{ia}, \triangle_{ib}, \triangle_{ja}, \triangle_{jb}, \triangle_{ka}, \triangle_{kb}\}$. Notice that here S is the same as the central small stencil S_0 in the type I reconstruction. Then we determine a

quadratic polynomial $p(x, y)$ by requiring that it has the same cell average as u on $\triangle_0$, and also it matches the cell averages of u on the triangles of the big stencil S except $\triangle_0$ in a least-square sense [1]. Notice that some of the second layer neighbors may coincide, but this does not affect the least-square procedure to determine $p(x, y)$. Let m denote the total number of cells in the big stencil S. If $m < 6$, there is no enough information for constructing a quadratic polynomial. Then we must go to the next neighboring layer and include more cells into the big stencil S. For every quadrature point (x^G, y^G), we compute a series of constants $\{c_l\}_{l=1}^m$ which depend on the local geometry only, such that

$$p(x^G, y^G) = \sum_{l=1}^{m} c_l \bar{u}_l \tag{2.10}$$

where every constant c_l corresponds to one cell in the big stencil S, and $\bar{u}_l$ is the cell average of u on that cell.

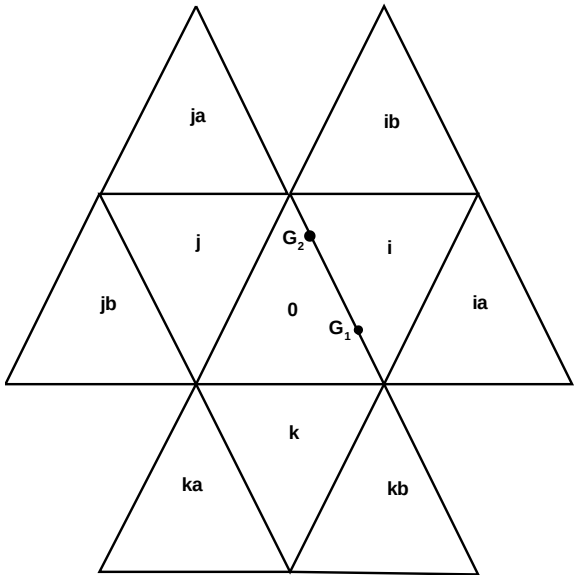

Figure 2.2: A big stencil S for a third order type II WENO reconstruction.

The key step in building a high order type II WENO scheme is to construct lower order polynomials whose weighted average will give the same result as the high order reconstruction at each quadrature point. This is the most difficult step for type II WENO schemes on unstructured meshes. The benefit by doing this is that type II WENO schemes have much

more compact stencils than type I WENO schemes. We use several linear polynomials to give the lower order reconstructions in the third order WENO reconstruction.

Using the big stencil S in Figure 2.2, we have 9 small stencil candidates and the corresponding 9 linear polynomials by agreeing with the cell averages of u on these small stencils. They are listed as following.

$$p_1^1(x,y) : S_1 = \{\triangle_0, \triangle_j, \triangle_k\}, \qquad p_2^1(x,y) : S_2 = \{\triangle_0, \triangle_k, \triangle_i\}, \qquad p_3^1(x,y) : S_3 = \{\triangle_0, \triangle_i, \triangle_j\},$$
$$p_4^1(x,y) : S_4 = \{\triangle_0, \triangle_i, \triangle_{ia}\}, \qquad p_5^1(x,y) : S_5 = \{\triangle_0, \triangle_i, \triangle_{ib}\}, \qquad p_6^1(x,y) : S_6 = \{\triangle_0, \triangle_j, \triangle_{ja}\},$$
$$p_7^1(x,y) : S_7 = \{\triangle_0, \triangle_j, \triangle_{jb}\}, \qquad p_8^1(x,y) : S_8 = \{\triangle_0, \triangle_k, \triangle_{ka}\}, \qquad p_9^1(x,y) : S_9 = \{\triangle_0, \triangle_k, \triangle_{kb}\}.$$

Notice that we use 9 small stencils instead of grouping them as in [11]. Our purpose by doing this is to test a general procedure for dealing with very general including highly distorted unstructured meshes. And this procedure proposed in this paper could be straightforwardly extented to higher order WENO schemes and 3D tetrahedral meshes.

For every quadrature point (x^G, y^G), on every small stencil S_i we compute three constants $\{c_l^{(i)}\}_{l=1}^3$ which depend on the local geometry only, such that

$$p_i^1(x^G, y^G) = \sum_{l=1}^{3} c_l^{(i)} \bar{u}_l^{(i)} \tag{2.11}$$

where every constant $c_l^{(i)}$ corresponds to one cell in the small stencil S_i, and $\bar{u}_l^{(i)}$ is the cell average of u on that cell.

Since a quadratic polynomial $p(x,y)$ has three more degrees of freedom than each linear polynomial $p_i^1(x,y)$, namely $\xi^2, \eta^2, \xi\eta$, where $\xi = (x - x_0)/h$ and $\eta = (y - y_0)/h$ are the scaled local basis functions on the target cell $\triangle_0$ with the barycenter (x_0, y_0) and $h = \sqrt{|\triangle_0|}$. For the degrees of freedom $1, \xi, \eta$, both the quadratic polynomial reconstruction and linear polynomial reconstruction can reproduce them exactly. To obtain the linear weights $\{\gamma_i\}_{i=1}^9$, we form the linear system at every Gaussian quadrature point (x^G, y^G): take $u = \xi^2, \eta^2, \xi\eta$ respectively, the equalities are:

$$\sum_{i=1}^{9} \gamma_i p_i^1(x^G, y^G) = u(x^G, y^G) \tag{2.12}$$

where p_i^1 is the linear reconstruction polynomial for u, using the small stencil S_i. Together with the requirement

$$\sum_{i=1}^{9} \gamma_i = 1, \tag{2.13}$$

we obtain a 4×9 linear system

$$A\gamma = b, \tag{2.14}$$

where $A \in R^{4\times 9}$, and $b \in R^4$. This is an under-determined system and there are infinitely many solutions. We define the optimal linear weights $\{\gamma_i\}_{i=1}^9$ as following. The third order reconstruction by the linear combination of the second order reconstructions using the optimal linear weights $\{\gamma_i\}_{i=1}^9$ is the "closest" one from the third order reconstruction by the big stencil S, in the least square sense. We form the linear system

$$M\gamma \stackrel{l}{=} c, \tag{2.15}$$

where $\stackrel{l}{=}$ means that the equality holds in the least square sense, and $M \in R^{m\times 9}$, $c \in R^m$. The vector $c = (c_1, c_2, \cdots, c_m)^T$, and $\{c_l\}_{l=1}^m$ are the approximation constants in (2.10) for the big stencil. Each column of the matrix M corresponds to the approximation constants in (2.11) for one of the small stencils. The systems (2.14) and (2.15) are solved together to give the optimal linear weights $\{\gamma_i\}_{i=1}^9$. Then we have obtained a type II third order linear reconstruction

$$p(x^G, y^G) \stackrel{l}{=} \sum_{i=1}^{9} \gamma_i p_i^1(x^G, y^G). \tag{2.16}$$

Note that the equation (2.16) holds in the least square sense.

2.2.3 Hybrid WENO reconstruction

It is obvious that the big stencil of a type II WENO scheme (Figure 2.2) is much more compact than that of a same order type I WENO scheme (Figure 2.1). Here the first one is just the central small stencil of the second one. However, when the spatial domain has high dimension and complex geometry, the quality of the unstructured meshes is hard to control. Distorted local mesh geometries are generated. This leads to very negative linear weights in

type II WENO schemes, or even the linear weights do *not* exist. For mild negative linear weights, the splitting technique developed in [18] can be applied effectively. For the case that linear weights are very negative large or do *not* exist, we propose a more robust approach in this section. Here we hybrid the approaches of type II and type I WENO schemes, and avoid the appearance of very negative large linear weights. Since for a general triangulation, distorted mesh geometries only occur in small parts of the whole domain. Hence type II WENO schemes can be applied for the major parts of the domain. At the places where the linear weights of the type II WENO reconstructions do *not* exist or are larger than a preset threshold value, the type I WENO reconstructions are applied. We summarize the hybrid WENO reconstruction algorithm at a Gaussian point in the following.

To form WENO reconstructions of the numerical values at a quadrature point (x^G, y^G) in the Lax-Friedrichs flux (2.4):

1. Calculate linear weights $\{\gamma_i\}_{i=1}^9$ in type II linear reconstruction (2.16), using the method described in section 2.2.2. If such linear weights do *not* exist, then go to step 3.

2. For a preset threshold value ζ, if $\max\{|\gamma_i|, i = 1, 2, ..., 9\} \leq \zeta$, then we form a WENO reconstruction (2.6) using the type II linear reconstruction (2.16). And the splitting technique in [18] is applied if $\min(\gamma_1, \cdots, \gamma_9) < 0$.

3. If $\max\{|\gamma_i|, i = 1, 2, ..., 9\} > \zeta$ or type II linear weights do *not* exist, then we form a WENO reconstruction (2.6) using the type I linear reconstruction (2.9) described in section 2.2.1.

Remark: Via numerical experiments in the next section, we find that the numerical results are *not* sensitive with respect to the choice of the threshold value ζ when ζ is in the range from 1 to 10. Hence a value of ζ between 1 to 10 is recommended for all numerical examples in this paper. If ζ is chosen to be bigger than 10, we observe an increase in

accuracy errors and loss of numerical accuracy order in the numerical experiments with distorted meshes.

3 Numerical examples

In this section, we apply the hybrid WENO reconstructions developed in the section 2 to both linear and non-linear scalar and system problems. We use triangular meshes with large obtuse angle mesh structures in the accuracy test problems. This kind of meshes gives very large negative linear weights in type II WENO reconstructions. They are used to show the robustness of the hybrid WENO reconstructions. The CFL number is taken as 0.3 in all the cases. For the temporal discretization, we use the third-order TVD Runge-Kutta scheme of Shu and Osher in [19]. To improve the accuracy of the WENO scheme, we adopt a mapped weights technique introduced in [10]. In the numerical convergence studies, we measure the discrete L^1 and L^∞ errors and convergence orders. The discrete L^1 and L^∞ errors at a final time T are calculated from the point errors at the Gaussian quadrature points in the finite volume scheme. Namely, we use the point errors at these Gaussian quadrature points $G_j^{(k)}$ in (2.3) to approximate the integral in the L^1 error and to find the maximum value in the L^∞ error.

Example 1. Linear equation:

$$\begin{cases} u_t + u_x + u_y = 0, & -2 \le x \le 2, -2 \le y \le 2; \\ u(x, y, 0) = \sin(\frac{\pi}{2}(x + y)), \end{cases} \tag{3.1}$$

with periodic boundary condition. We use random perturbations of unform meshes to generate meshes with large obtuse angles and test our hybrid WENO reconstructions. This kind of meshes generate large negative linear weights in the type II WENO reconstructions. See Figure (3.1) for two of such meshes. In the convergence study, the refinement of meshes is done by cutting each triangle into four smaller similar ones. We use the hybrid WENO schemes to solve the PDE (3.1) to $T = 2$. First we use successively refined meshes of the left mesh in Figure (3.1) to test the accuracy and numerical convergence orders. The results are

reported in Table 3.1 and Table 3.2, for different preset threshold value $\zeta = 1$ and $\zeta = 10$ respectively. We also report the most negative linear weight in type II WENO reconstructions on every mesh, and the percentage of using type I WENO reconstructions on Gaussian points. We would like to point out that the most negative linear weight is determined by the meshes only, hence the same mesh generates the same most negative linear weight, as shown in Tables of this example and the next example. From Table 3.1 and Table 3.2, we can observe third order accuracy in L^1 and L^∞ errors, although the most negative linear weight is around -200. Furthermore, the percentage of using type I WENO reconstructions is very small, and it is decreasing when the mesh is refined. This is because the percentage of "bad" quality triangles is still small. Hence at most of places, we are still using compact type II WENO reconstructions. Notice that, L^∞ errors are slightly larger than L^1 errors, and L^∞ convergence orders are not as uniform as L^1 convergence orders. This is due to the highly non-uniform of the meshes. Comparing Table 3.1 and Table 3.2, we can see that the accuracy and convergence orders are comparable. With the tests of other ζ values (not shown here), we found that the accuracy and orders are not sensitive with respect to the preset threshold value ζ when its value is less than 10. With bigger ζ values, we use even less type I WENO reconstructions. Then we perform the convergence studies using even worse quality meshes which are refined meshes of the right mesh in Figure (3.1). The results are reported in Table 3.3 and Table 3.4. For these meshes, the most negative linear weight can reach -8000. From the results, we can see that our hybrid approach still performs very well and similar conclusion can be obtained.

Table 3.1: Accuracy for 2D Linear Equation. Computational meshes are refined meshes of the left mesh in Figure (3.1). $\zeta = 1.0$.

# of cells	L^1 error	Order	L^∞ error	Order	most negative weight	percentage
10368	0.107E-02	–	0.747E-02	–	-199.72	1.19%
41472	0.109E-03	3.30	0.307E-03	4.60	-199.88	0.59%
165888	0.137E-04	2.99	0.470E-04	2.71	-200.53	0.29%
663552	0.172E-05	2.99	0.775E-05	2.60	-201.20	0.15%

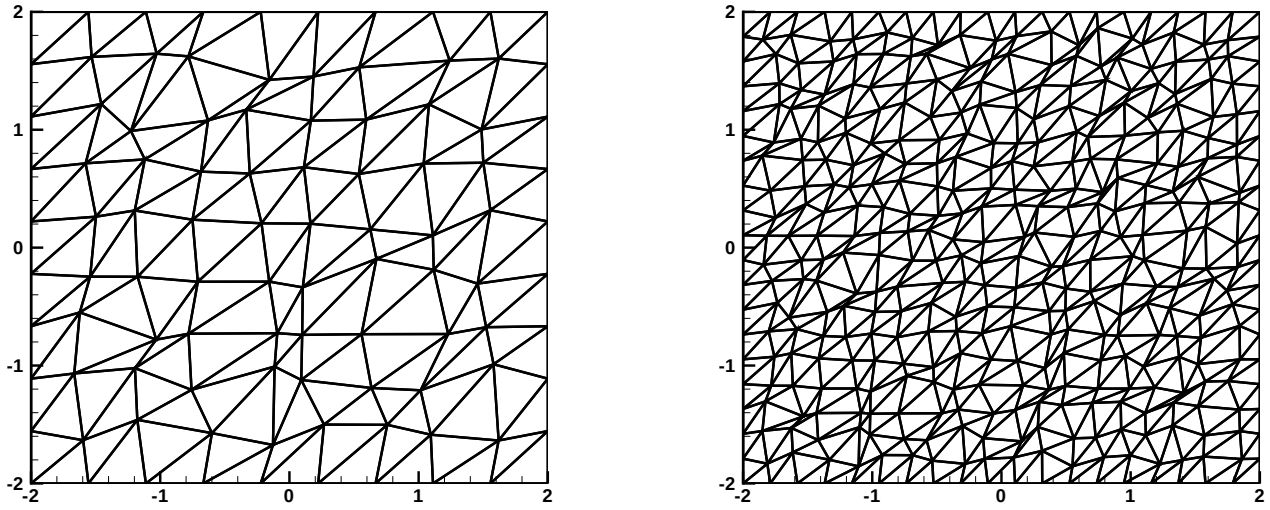

Figure 3.1: Coarsest meshes in the convergence study. Left: the mesh is obtained by randomly perturbing a 10×10 uniform mesh within $\pm 30\%$ for every interior node; Right: the mesh is obtained by randomly perturbing a 20×20 uniform mesh within $\pm 35\%$ for every interior node.

Table 3.2: Accuracy for 2D Linear Equation. Computational meshes are refined meshes of the left mesh in Figure (3.1). $\zeta = 10.0$.

# of cells	L^1 error	Order	L^∞ error	Order	most negative weight	percentage
10368	0.107E-02	–	0.754E-02	–	-199.72	0.13%
41472	0.109E-03	3.30	0.299E-03	4.66	-199.88	0.06%
165888	0.137E-04	2.99	0.458E-04	2.71	-200.53	0.03%
663552	0.172E-05	2.99	0.778E-05	2.56	-201.20	0.02%

Table 3.3: Accuracy for 2D Linear Equation. Computational meshes are refined meshes of the right mesh in Figure (3.1). $\zeta = 1.0$.

# of cells	L^1 error	Order	L^∞ error	Order	most negative weight	percentage
11552	0.945E-03	–	0.633E-02	–	-5426.19	3.44%
46208	0.104E-03	3.18	0.357E-03	4.15	-5574.93	1.72%
184832	0.130E-04	3.00	0.478E-04	2.90	-6457.42	0.86%
739328	0.164E-05	2.99	0.672E-05	2.83	-8006.47	0.43%

Example 2. Nonlinear Burgers' equation:

$$u_t + (\frac{u^2}{2})_x + (\frac{u^2}{2})_y = 0 \tag{3.2}$$

Table 3.4: Accuracy for 2D Linear Equation. Computational meshes are refined meshes of the right mesh in Figure (3.1). $\zeta = 10.0$.

# of cells	L^1 error	Order	L^∞ error	Order	most negative weight	percentage
11552	0.951E-03	–	0.652E-02	–	-5426.19	0.35%
46208	0.103E-03	3.21	0.358E-03	4.18	-5574.93	0.18%
184832	0.130E-04	2.99	0.478E-04	2.90	-6457.42	0.09%
739328	0.164E-05	2.99	0.671E-05	2.83	-8006.47	0.04%

with the initial condition

$$u_0(x, y) = 0.3 + 0.7 \sin(\frac{\pi}{2}(x + y)) \tag{3.3}$$

$(x, y) \in [-2, 2] \times [-2, 2]$, with periodic boundary condition. We apply the hybrid WENO schemes to solve the PDE (3.2) to $T = 0.5/\pi^2$, when the solution is still smooth. Again we used the same meshes with large obtuse angles as those in Example 1. Numerical results are reported in Table 3.5, Table 3.6, Table 3.7 and Table 3.8. We observe good third order accuracy and the same conclusion can be obtained as that in Example 1.

Table 3.5: Accuracy for 2D Burgers Equation. Computational meshes are refined meshes of the left mesh in Figure (3.1). $\zeta = 1.0$.

# of cells	L^1 error	Order	L^∞ error	Order	most negative weight	percentage
10368	0.106E-03	–	0.116E-02	–	-199.72	1.19%
41472	0.125E-04	3.08	0.164E-03	2.82	-199.88	0.59%
165888	0.159E-05	2.97	0.236E-04	2.80	-200.53	0.29%
663552	0.201E-06	2.98	0.378E-05	2.64	-201.20	0.15%

Table 3.6: Accuracy for 2D Burgers Equation. Computational meshes are refined meshes of the left mesh in Figure (3.1). $\zeta = 10.0$.

# of cells	L^1 error	Order	L^∞ error	Order	most negative weight	percentage
10368	0.107E-03	–	0.112E-02	–	-199.72	0.13%
41472	0.125E-04	3.10	0.157E-03	2.83	-199.88	0.06%
165888	0.159E-05	2.97	0.233E-04	2.75	-200.53	0.03%
663552	0.201E-06	2.98	0.374E-05	2.64	-201.20	0.02%

Table 3.7: Accuracy for 2D Burgers Equation. Computational meshes are refined meshes of the right mesh in Figure (3.1). $\zeta = 1.0$.

# of cells	L^1 error	Order	L^∞ error	Order	most negative weight	percentage
11552	0.101E-03	–	0.193E-02	–	-5426.19	3.44%
46208	0.120E-04	3.07	0.195E-03	3.30	-5574.93	1.72%
184832	0.157E-05	2.93	0.301E-04	2.70	-6457.42	0.86%
739328	0.203E-06	2.95	0.490E-05	2.62	-8006.47	0.43%

Table 3.8: Accuracy for 2D Burgers Equation. Computational meshes are refined meshes of the right mesh in Figure (3.1). $\zeta = 10.0$.

# of cells	L^1 error	Order	L^∞ error	Order	most negative weight	percentage
11552	0.103E-03	–	0.576E-02	–	-5426.19	0.35%
46208	0.120E-04	3.10	0.178E-03	5.02	-5574.93	0.18%
184832	0.157E-05	2.93	0.270E-04	2.72	-6457.42	0.09%
739328	0.203E-06	2.95	0.438E-05	2.62	-8006.47	0.04%

Example 3. (2D vortex evolution problem [11].) We solve the compressible Euler equations of gas dynamics :

$$\xi_t + f(\xi)_x + g(\xi)_y = 0, \tag{3.4}$$

where

$$\xi = (\rho, \rho u, \rho v, E),$$

$$f(\xi) = (\rho u, \rho u^2 + p, \rho uv, u(E + p)),$$

$$g(\xi) = (\rho v, \rho uv, \rho v^2 + p, v(E + p)).$$

Here ρ is the density, (u, v) is the velocity, E is the total Energy, p is the pressure, and

$$E = \frac{p}{\gamma - 1} + \frac{1}{2}\rho(u^2 + v^2),$$

with $\gamma = 1.4$. The mean flow is $\rho = 1, p = 1$, and $(u, v) = (1, 1)$. An isentropic vortex is added to the mean flow, i.e., perturbations in (u, v) and the temperature $T = \frac{p}{\rho}$, no perturbation in the entropy $S = \frac{p}{\rho^\gamma}$:

$$(\delta u, \delta v) = \frac{\epsilon}{2\pi} e^{0.5(1-r^2)}(-\bar{y}, \bar{x})$$

$$\delta T = -\frac{(\gamma-1)\epsilon^2}{8\gamma\pi^2} e^{1-r^2}, \qquad \delta S = 0,$$

where $(\bar{x}, \bar{y}) = (x-5, y-5), r^2 = \bar{x}^2 + \bar{y}^2$, and the vortex strength $\epsilon = 5$. The computational domain is taken as $[0, 10] \times [0, 10]$, and periodic boundary conditions are used. Solution of the system is smooth, hence it is often used as a benchmark problem for testing accuracy of numerical schemes for solving Euler systems. We use the mesh shown in Figure 3.2 and its refined ones to test the accuracy of our hybrid WENO scheme. The final time $T = 2.0$. Numerical results are reported in Table 3.9 and Table 3.10. Again, we observe good third order accuracy and the same conclusion is obtained as that in the previous examples.

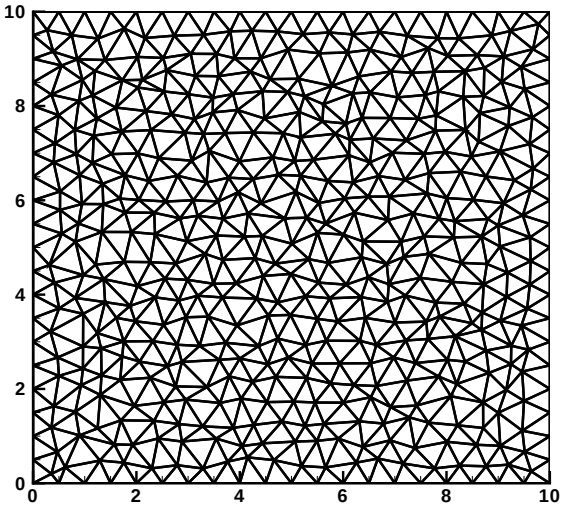

Figure 3.2: The coarsest mesh in the convergence study for the vortex evolution problem.

Table 3.9: Accuracy for 2D Vortex Evolution Problem, $\zeta = 1.0$.

# of cells	L^1 error	Order	L^∞ error	Order	most negative weight	percentage
928	0.808E-02	–	0.171E+00	–	-380.02	7.94%
3712	0.213E-02	1.92	0.610E-01	1.49	-487.20	5.35%
14848	0.391E-03	2.45	0.215E-01	1.50	-486.50	2.74%
59392	0.319E-04	3.62	0.630E-03	5.09	-486.35	1.39%
237568	0.405E-05	2.98	0.807E-04	2.96	-485.37	0.70%
950272	0.541E-06	2.90	0.120E-04	2.75	-495.94	0.35%

Table 3.10: Accuracy for 2D Vortex Evolution Problem. $\zeta = 10.0$.

# of cells	L^1 error	Order	L^∞ error	Order	most negative weight	percentage
928	0.958E-02	–	0.172E+00	–	-380.02	0.83%
3712	0.252E-02	1.93	0.681E-01	1.34	-487.20	0.61%
14848	0.403E-03	2.64	0.237E-01	1.52	-486.50	0.29%
59392	0.318E-04	3.66	0.632E-03	5.23	-486.35	0.14%
237568	0.405E-05	2.97	0.806E-04	2.97	-485.37	0.07%
950272	0.541E-06	2.90	0.119E-04	2.76	-495.94	0.04%

Example 4. (Double mach reflection problem [21].) We solve the Euler equations (3.4) in a computational domain $[0, 3.2] \times [0, 1]$. A reflecting wall lies at the bottom of the domain starting from $x = \frac{1}{6}$. Initially a right moving Mach 10 shock is located at $x = \frac{1}{6}, y = 0$, making a 60° angle with the x axis. The reflective boundary condition is used at the wall. The exact postshock condition is imposed for the rest of the bottom boundary (i.e., the part from $x = 0$ to $x = \frac{1}{6}$). At the top boundary, the flow values are set to describe the exact motion of the Mach 10 shock. The final time is $T = 0.2$.

We randomly perturbe the uniform computational meshes with equilateral triangles in [11] within $\pm 10\%$ for every interior node, and use the hybrid WENO reconstructions to perform simulations on successively refined meshes. The most negative weights in type II WENO reconstructions for these meshes are about -100. We observed the convergence of the numerical solution. Here we present the numerical solution in Figure 3.3 for the most refined mesh (side length of each triangle in the mesh is roughly equal to rectangular element case of $\Delta x = \Delta y = \frac{1}{400}$). We compare the results by using different threshold values $\zeta = 1$ and $\zeta = 10$. For $\zeta = 1$, the percentage of using type I WENO reconstructions is 0.10%, while it is 0.02% for $\zeta = 10.0$. The results are similar for different threshold values, and they are comparable with the results in [11] by using the uniform computational meshes.

Example 5. (A hyperbolic model for chemosensitive movement [5].) We apply the third order hybrid WENO method to solve a hyperbolic model for cell chemosensitive movement. The model was developed in [8]. In [5], a high order finite difference WENO scheme was

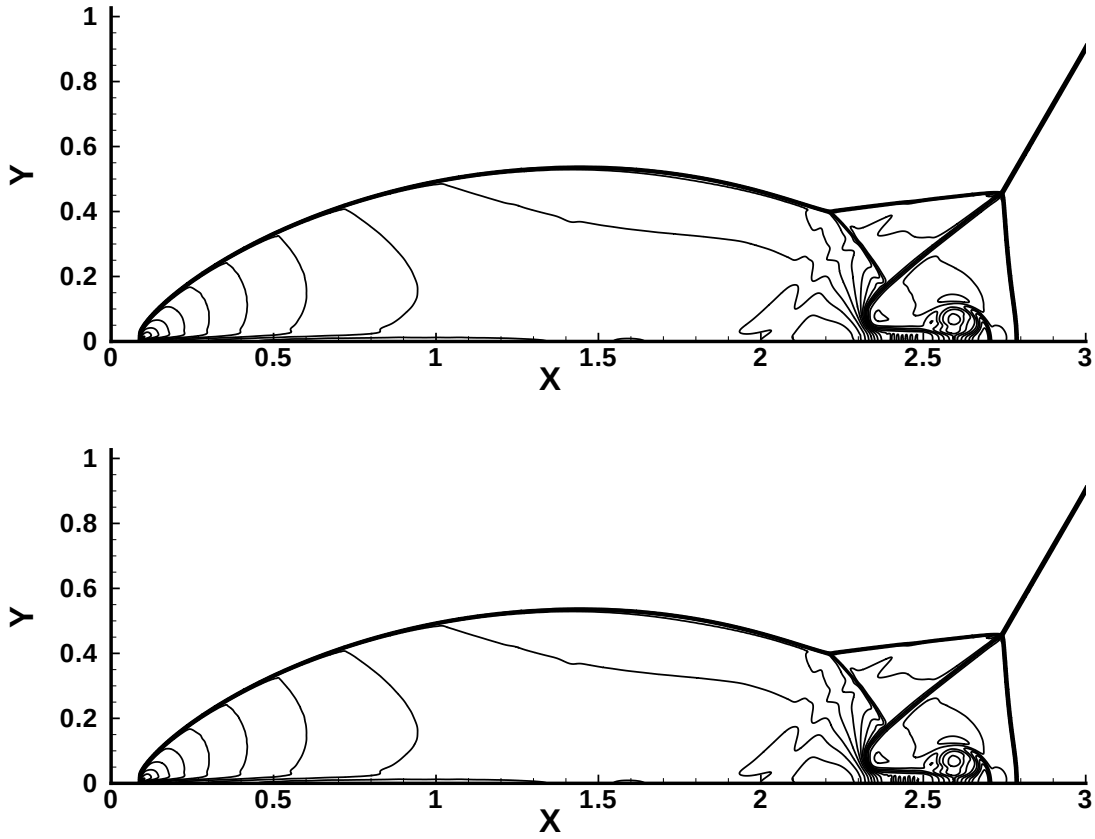

Figure 3.3: Double mach reflection. Density contours with 30 equally spaced contour lines from 1.5 to 21.5. Top: $\zeta = 1$; bottom: $\zeta = 10$.

constructed to simulate it. The model equations are

$$\begin{cases} \dfrac{\partial n}{\partial t} + \nabla \cdot (n\vec{v}) = 0; \\ \dfrac{\partial \vec{v}}{\partial t} + \vec{v} \cdot \nabla \vec{v} = \beta \nabla c; \\ \dfrac{\partial c}{\partial t} = D \triangle c + \alpha n - \dfrac{c}{\tau}, \end{cases} \tag{3.5}$$

where n denote the cell density, $\vec{v}$ is the velocity of cell movements. c is the concentration of chemicals secreted by the cells. β represents the strength of chemotactic interactions. The cell density n and velocity $\vec{v}$ satisfy hyperbolic conservation laws. Chemical concentration c satisfies a reaction-diffusion equation. D is the diffusion rate, α is the production rate, and $1/\tau$ is the degradation rate. We consider the 2D case $\vec{v} = (v_1, v_2)^T$, and write the system

(3.5) in a conservative form

$$\begin{cases} \dfrac{\partial n}{\partial t} + \dfrac{\partial (nv_1)}{\partial x} + \dfrac{\partial (nv_2)}{\partial y} = 0; \\ \dfrac{\partial (nv_1)}{\partial t} + \dfrac{\partial (nv_1^2)}{\partial x} + \dfrac{\partial (nv_1 v_2)}{\partial y} = n\beta \dfrac{\partial c}{\partial x}; \\ \dfrac{\partial (nv_2)}{\partial t} + \dfrac{\partial (nv_1 v_2)}{\partial x} + \dfrac{\partial (nv_2^2)}{\partial y} = n\beta \dfrac{\partial c}{\partial y}; \\ \dfrac{\partial c}{\partial t} = D(\dfrac{\partial^2 c}{\partial x^2} + \dfrac{\partial^2 c}{\partial y^2}) + \alpha n - \dfrac{c}{\tau}. \end{cases} \tag{3.6}$$

The first three equations in (3.6) is the hyperbolic part of the system, and we use the third order finite volume hybrid WENO method to solve them. The fourth equation is a parabolic equation, and we do not need to use WENO reconstruction. We use finite volume formulation in section 2.1 with the flux $F = -D\nabla c$. Different from the numerical flux (2.4) for hyperbolic PDEs, we use the average numerical flux

$$F(\nabla c(G_j^{(k)}, t)) \cdot n_k \approx \frac{1}{2} \left(F(\nabla c^-(G_j^{(k)}, t)) + F(\nabla c^+(G_j^{(k)}, t)) \right) \cdot n_k. \tag{3.7}$$

The gradient ∇p of reconstructed quadratic polynomial $p(x, y)$ for c on the big stencil (Figure 2.2) is directly used to approximate ∇c. We use the following parameters [8]:

$$\beta = 1.0, \qquad D = 2.0, \qquad \alpha = 1.0, \qquad \tau = 1.0. \tag{3.8}$$

We perform numerical simulations on both a square domain $[0, 20] \times [0, 20]$ and a circular domain with the center $(10, 10)$ and radius 10. Periodic boundary condition and non-flux boundary condition are used for the square domain and the circular domain respectively. Initially certain number of cells are randomly distributed in the domain. We assume that cells have shape of Gaussian bumps. So the initial cell density n is taken as a normalized superposition of randomly distributed Gaussian bumps with width $\sigma = 0.175$

$$n(x, y) = \frac{1}{(2\pi\sigma)^2} \sum_{i=1}^{N} \exp(-\frac{(x - x_i)^2 + (y - y_i)^2}{2\sigma^2}), \tag{3.9}$$

where $(x_i, y_i)_{1 \le i \le N}$ are uniformly distributed random points in the domain. N here represents the total number of cells, and $N = 10000$ is used in our simulation. The initial cell velocity

and chemical concentration are taken as 0. See Figure (3.4) for the initial cell density on two different domains. The domains are partitioned by triangular meshes with 144646 elements for the square domain, and 121592 elements for the circular domain. We use the third order hybrid WENO method to perform the simulations till $t = 1.56$, and again compare the results for $\zeta = 1$ and $\zeta = 10$. The triangular mesh for the square domain generates the most negative weight -1284 in the type II WENO reconstructions. In our simulations, only 0.15% of all elements (if $\zeta = 1$) and 0.01% of all elements (if $\zeta = 10$) use the type I WENO reconstructions. For the circular domain, the triangular mesh we use generates the most negative weight -333 in the type II WENO reconstructions, and 0.16% of all elements (if $\zeta = 1$) and 0.01% of all elements (if $\zeta = 10$) use the type I WENO reconstructions. See Figure (3.5) and Figure (3.6) for the simulation results on different domains. We can observe that network patterns similar to early blood vessel structures are generated. Again, different threshold values $\zeta = 1$ and $\zeta = 10$ generate similar numerical results.

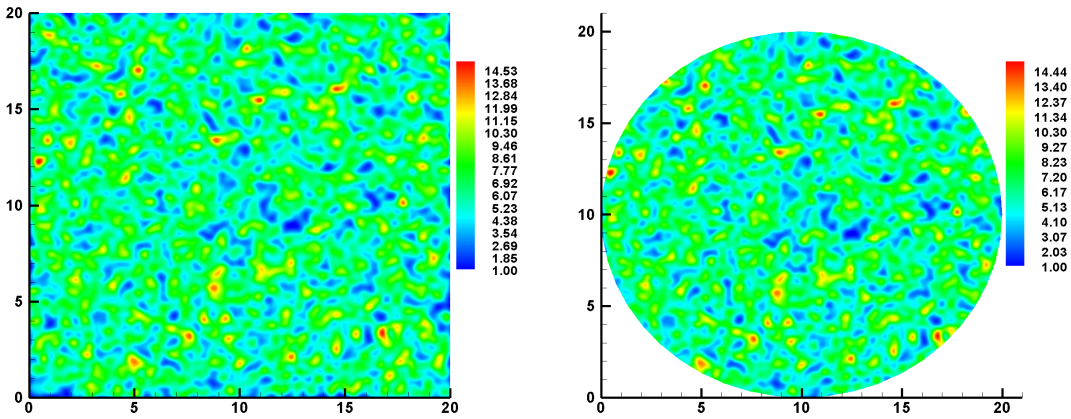

Figure 3.4: Initial cell density n. Left: the square domain; right: the circular domain.

4 Concluding remarks

A difficult step in designing robust high order type II WENO schemes on unstructured meshes is how to deal with ill-posed or singular systems for finding linear weights when

the mesh quality is not good. This problem is even more important in developing type II WENO schemes on higher dimensional unstructured meshes. In this paper, we solve this problem by hybriding the approaches of the type II and the type I WENO reconstructions. The resulting hybrid finite volume WENO reconstructions are robust in dealing with bad quality meshes. Although the compactness of the type II WENO reconstructions is lost at the places where mesh quality is bad, the overall percentage of the places where the type I WENO reconstructions are applied is quite small. Numerical experiments including both scalar and hyperbolic system cases show the robutness of our approach.

References

[1] T. Barth and P. Frederickson, *High order solution of the Euler equations on unstructured grids using quadratic reconstruction*, AIAA Paper No. 90-0013.

[2] M. Castro, B. Costa and W.S. Don, *High order weighted essentially non-oscillatory WENO-Z schemes for hyperbolic conservation laws*, Journal of Computational Physics, 230 (2011), pp. 1766-1792.

[3] M. Dumbser and M. Käser, *Arbitrary high order non-oscillatory finite volume schemes on unstructured meshes for linear hyperbolic systems*, Journal of Computational Physics, 221 (2007), pp.693-723.

[4] M. Dumbser, M. Käser, V.A. Titarev and E.F. Toro, *Quadrature-free non-oscillatory finite volume schemes on unstructured meshes for nonlinear hyperbolic systems*, Journal of Computational Physics, 226 (2007), pp. 204-243.

[5] F. Filbet and C.-W. Shu, *Approximation of hyperbolic models for chemosensitive movement*, SIAM J. Sci. Comput., Vol.27, No.3, (2005), pp850-872.

[6] T.C. Fisher, M.H. Carpenter, N.K. Yamaleev and S.H. Frankel, *Boundary closures for fourth-order energy stable weighted essentially non-oscillatory finite-difference schemes*, Journal of Computational Physics, 230 (2011), pp. 3727-3752.

[7] O. Friedrichs, *Weighted essentially non-oscillatory schemes for the interpolation of mean values on unstructured grids*, Journal of Computational Physics, 144 (1998), pp.194-212.

[8] A. Gamba, D. Ambrosi, A. Coniglio, A. De Candia, S. Di Talia, E. Diraudo, G. Serini, L. Preziosi and F. Bussolino, *Percolation, morphogenesis, and Burgers dynamics in blood vessels formation*, Physical Review Letters, 90, (2003), 118101.

[9] A. Harten, B. Engquist, S. Osher and S. Chakravarthy, *Uniformly high order essentially non-oscillatory schemes, III*, Journal of Computational Physics, 71 (1987), pp. 231-303.

[10] A.K. Henrick, T.D. Aslam and J.M. Powers, *Mapped weighted essentially non-oscillatory schemes: achieving optimal order near critical points*, Journal of Computational Physics, 207 (2005), pp.542-567.

[11] C. Hu and C.-W. Shu, *Weighted essentially non-oscillatory schemes on triangular meshes*, Journal of Computational Physics, 150 (1999), pp.97-127.

[12] G. Jiang and C.-W. Shu, *Efficient implementation of weighted ENO schemes*, Journal of Computational Physics, 126 (1996), pp.202-228.

[13] X.-D. Liu, S. Osher and T. Chan, *Weighted essentially non-oscillatory schemes*, Journal of Computational Physics, 115 (1994), pp.200-212.

[14] M. Motamed, C.B. Macdonald and S.J. Ruuth, *On the linear stability of the fifth-order WENO discretization*, Journal of Scientific Computing, 47 (2011), pp.127-149.

[15] J. Qiu and C.-W. Shu, *Runge-Kutta discontinuous Galerkin method using WENO limiters*, SIAM Journal on Scientific Computing, 26 (2005), pp.907-929.

[16] J. Qiu and C.-W. Shu, *Hermite WENO schemes and their application as limiters for Runge-Kutta discontinuous Galerkin method II: two dimensional case*, Computers and Fluids, 34 (2005), pp.642-663.

[17] S. Serna and A. Marquina, *Power ENO methods: a fifth-order accurate weighted power ENO method*, Journal of Computational Physics, 194 (2004), pp. 632-658.

[18] J. Shi, C. Hu and C.-W. Shu, *A technique of treating negative weights in WENO schemes*, Journal of Computational Physics, 175 (2002), pp.108-127.

[19] C.-W. Shu and S. Osher, *Efficient implementation of essentially non-oscillatory shock capturing schemes*, Journal of Computational Physics, 77 (1988), pp.439-471.

[20] V. A. Titarev, P. Tsoutsanis and D. Drikakis, *WENO schemes for mixed-element unstructured meshes*, Communications in Computational Physics, 8 (2010), pp. 585-609.

[21] P. Woodward and P. Colella, *The numerical simulation of two-dimensional fluid flow with strong shocks*, Journal of Computational Physics, 54 (1984), pp.115-173.

[22] S. Zhang and C.-W. Shu, *A new smoothness indicator for the WENO schemes and its effect on the convergence to steady state solutions*, Journal of Scientific Computing, 31 (2007), pp.273-305.

[23] Y.-T. Zhang and C.-W. Shu, *High order WENO schemes for Hamilton-Jacobi equations on triangular meshes*, SIAM Journal on Scientific Computing, 24 (2003), pp.1005-1030.

[24] Y.-T. Zhang and C.-W. Shu, *Third order WENO schemes on three dimensional tetrahedral meshes*, Communications in Computational Physics, 5 (2009), pp. 836-848.

[25] J. Zhu, J. Qiu, C.-W. Shu and M. Dumbser, *Runge-Kutta discontinuous Galerkin method using WENO limiters II: Unstructured meshes*, Journal of Computational Physics, 227 (2008), pp. 4330-4353.

[26] J. Zhu and J. Qiu, *Hermite WENO schemes and their application as limiters for Runge-Kutta discontinuous Galerkin method III: Unstructured meshes*, Journal of Scientific Computing, 39 (2009), 293-321.

[27] J. Zhu and J. Qiu, *Runge-Kutta discontinuous Galerkin method using WENO type limiters: Three dimensional unstructured meshes*, Communications in Computational Physics, to appear.

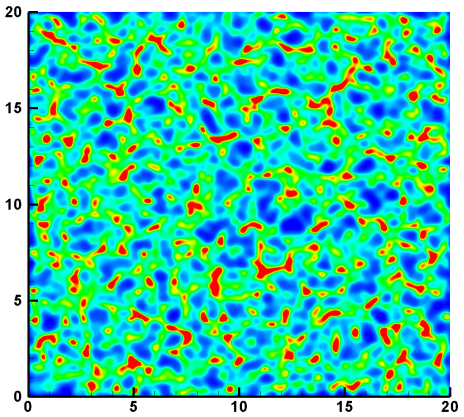

(a)

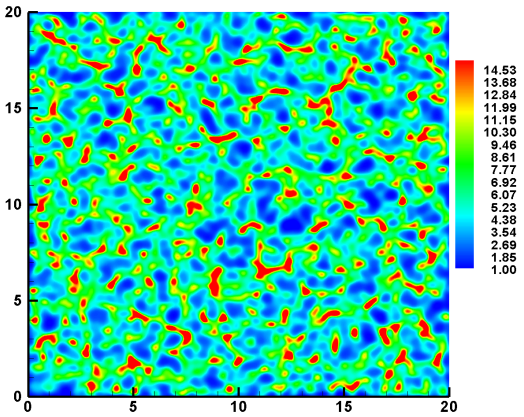

(b)

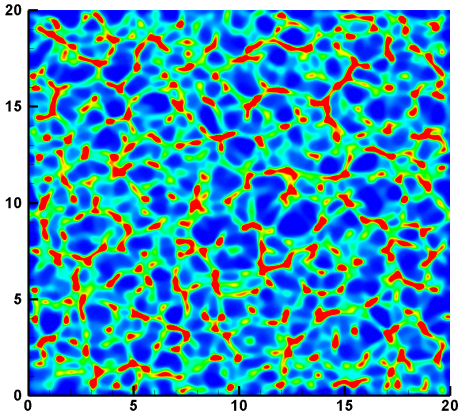

(c)

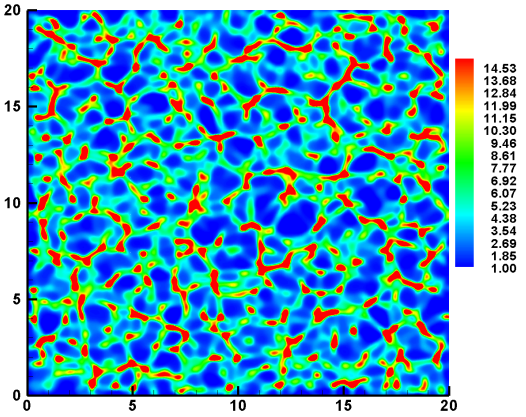

(d)

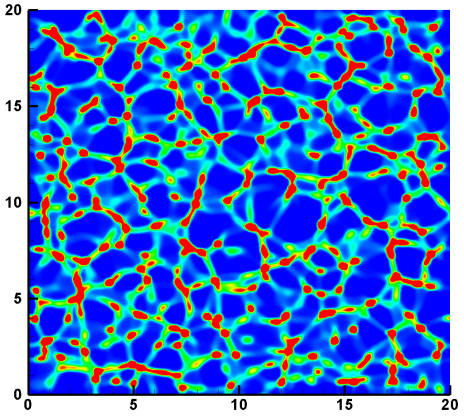

(e)

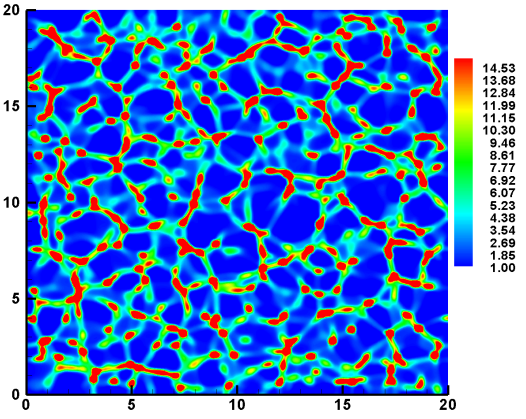

(f)

Figure 3.5: Numerical simulations of the cell density evolution. (a)(b): t = 0.76; (c)(d): t = 1.16; (e)(f): t = 1.56. (a)(c)(e): $\zeta = 1$; (b)(d)(f): $\zeta = 10$.

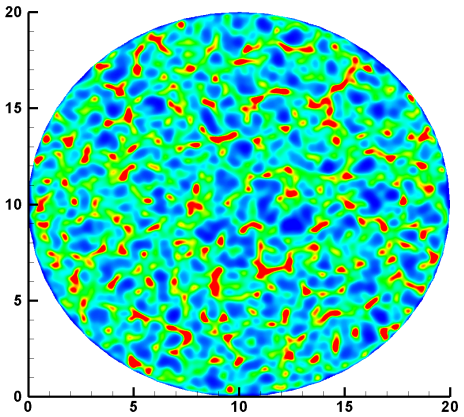

(a)

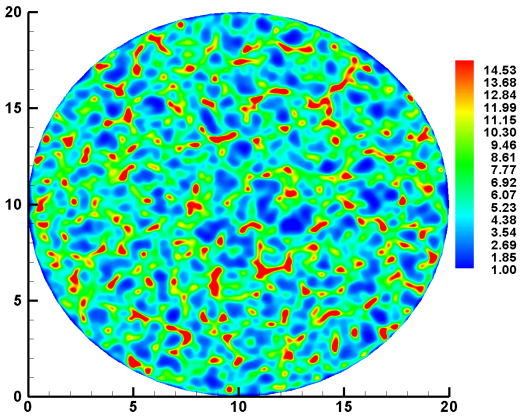

(b)

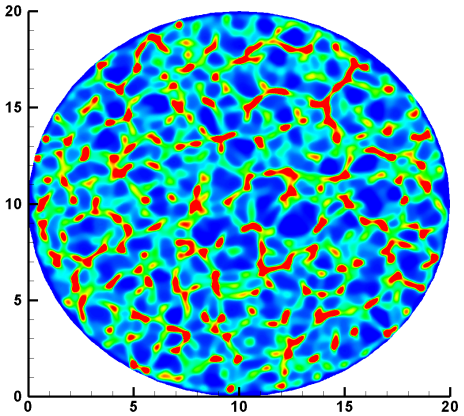

(c)

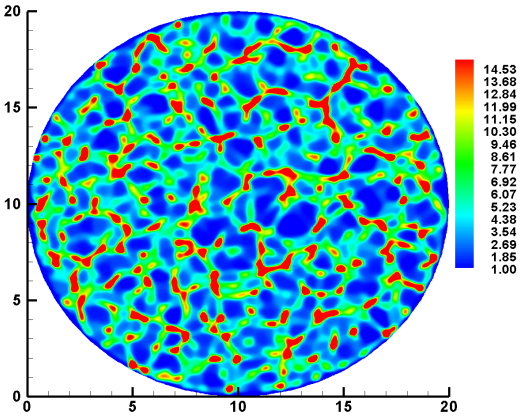

(d)

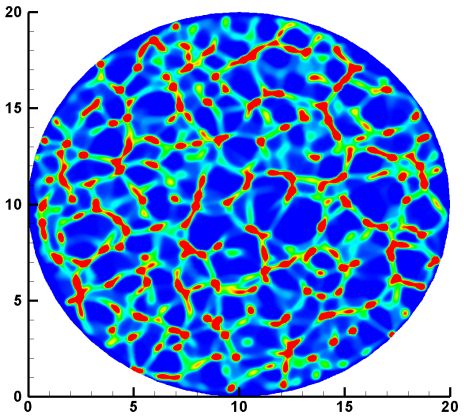

(e)

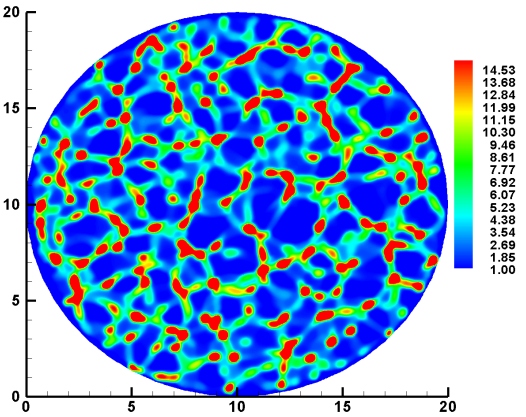

(f)

Figure 3.6: Numerical simulations of the cell density evolution. (a)(b) t = 0.76; (c)(d) t = 1.16; (e)(f) t = 1.56. (a)(c)(e): $\zeta = 1$; (b)(d)(f): $\zeta = 10$.